Geochemistry, Geophysics, Geosystems

Supporting Information for

Crust and Upper Mantle Structure Beneath the Eastern United States

Chengping Chai[1], Charles J. Ammon[2], Monica Maceira[1], Robert Herrmann[3]

[1]Oak Ridge National Laboratory, Oak Ridge, Tennessee, U.S.A.

[2]Department of Geosciences, Pennsylvania State University, University Park, Pennsylvania, U.S.A.

[3]Department of Earth and Atmospheric Sciences, Saint Louis University, St. Louis, Missouri, U.S.A.

Contents of this file

Additional Supporting Information (Files uploaded separately)

Introduction

This supplement includes details on the formulas to convert seismic velocities to densities (Text S1); paragraphs describing cross-sections B1-B2, D1-D2, E1-E2, F1-F2, G1-G2, and H1-H2 (Text S2); a map showing the seismic stations used for receiver functions (Figure S1); a map showing the seismic events used for receiver functions (Figure S2); a figure showing the relative data variance of receiver functions (Figure S3); a figure showing example surface-wave dispersions (Figure S4); a figure showing Bouguer

gravity maps before and after wavenumber filtering (Figure S5); a comparison of single-station receiver functions and smoothed receiver functions (Figure S6); a figure showing the convergence of the simultaneous inversion (Figure S7); a figure showing receiver function misfits (Figure S8); a figure showing surface-wave dispersion misfits (Figure S9); a comparison of the observed gravity maps and the predicted gravity maps (Figure S10); a comparison of EARS crust thickness before and after smoothing (Figure S11); a comparison of crustal thickness maps from recent seismic velocity models (Figure S12); a comparison of 1D velocity profiles (Figure S13); a figure showing the distributions of crustal and uppermost mantle P-wave velocities (Figure S14); a comparison of the uppermost mantle V_s and earthquake focal mechanisms (Figure S15); a comparison of the upper mantle shear speed at 63 km depth in western and easter U.S. (Figure S16); maps showing cluster locations (Figure S17 and S19); velocity profiles for each cluster (Figure S18 and S20); Rayleigh wave sensitivity kernels (Figure S21); V_s cross-section C1-C2 (Figure S22); V_s cross-section D1-D2 (Figure S23); V_s cross-section E1-E2 and F1-F2 (Figure S24); V_s cross-section G1-G2 and H1-H2 (Figure S25); the final seismic velocity model for the eastern United States in a text file (Data Set S1); the seismic velocity model for the western United States in a text file (Data Set S2); a list of seismic networks used in an excel file (Table S1); an animation compares the single-station-averaged receiver functions and the smoothed version (Movie S1); and interactive tools to view the seismic velocity model for the eastern United States (Visualization S1) and for the western United States (Visualization S2).

Text S1.

We used the following formulas from Maceira & Ammon (2009) to convert seismic velocities to densities.

$$\rho(\alpha) = \cos^2\phi\,\rho_2(\alpha) + \sin^2\phi\,\rho_1(\alpha)$$

$$\rho_1(\alpha) = \frac{\alpha + 2.40}{3.125}$$

$$\rho_2(\alpha) = \frac{7.55 - \sqrt{57.00 - 10.56(6.86 - \alpha)}}{5.28}$$

$$\phi = \frac{\pi}{2}\frac{1 + \tanh[\xi(\alpha - \alpha_c)]}{2}$$

In the formulas, ξ is 0.5 and α_c is 6.2 km/s. α is the seismic P wave velocity in km/s and ρ is density in g/cm^3.

Text S2.

The cross-section C1-C2 (Figure S22) is parallel to the longer arm of the New Madrid seismic zone (NMSZ) and passes through the Wabash Valley seismic zone (WVSZ) of Illinois and Indiana. Compared to the region to the north (left in Figure), the crust hosting modern WVSZ seismicity is relatively faster, with a smaller velocity gradient in the mid-to-lower crust. The WVSZ is underlain by a slightly thicker crust than the NMSZ. However, the upper mantle beneath the WVSZ is faster than that beneath the NMSZ. A broad higher velocity anomaly is imaged beneath the WVSZ about 70-150 km depth, which agrees with a recent local study (Chen Chen et al., 2016). The continuation of a

relatively fast lower crust beneath the NMSZ northward to the WVSZ may suggest these two seismic active regions are connected (Chen Chen et al., 2016). To the south-southwest of the NMSZ, deeper into the Mississippi Embayment, the sedimentary cover thickens to at least 10 km and the crust thins to roughly 30 km.

The cross-section D1-D2, E1-E2, F1-F2, G1-G2, and H1-H2 pass through and across the Appalachian Mountains. Cross-section D1-D2 (Figure S23) clearly shows a slower upper mantle beneath New England, which is consistent with other studies (Pollitz & Mooney, 2016; Schmandt et al., 2015; Shen & Ritzwoller, 2016). The decrease seismic velocity has been interpreted as due to interaction with the Great Meteor hotspot roughly 50 Ma (Eaton & Frederiksen, 2007). Along the profile, which samples the Valley and Ridge Province of central and eastern Pennsylvania, the crustal thickness increases by roughly 10 km from eastern Pennsylvania into the West-Virginia border. Crustal thicknesses in western Pennsylvania are comparable to those to the south (see Figure 5). Although the mid crust varies in speed along the profile, the change in crustal thickness appears to arise from an increase in thickness of lower crustal material. Depths of earthquakes along the profile are generally above 25 kilometers and show no systematic variation with the structure.

Cross-section E1-E2 (Figure S24) samples from southeastern Canada into New England and crosses the West Quebec seismic zone (WQSZ). Magnitude 3 and larger earthquakes extend to 20 km depth in the WQSZ region and appear to shallow slightly along the profile in New York and New England. Along this direction, the WQSZ locates near the edge of the Canadian Shield as is evident in the mantle speed cross-section. Cross-section F1-F2 (Figure S24) shows a crustal thickness change beneath central Pennsylvania. Crossing from the Appalachian Plateau to the Valley and Ridge Province, the upper crust slows and the lower crust thins. At roughly the same position the mantle speeds decrease. Seismicity in the region shows transitions from reverse faulting in the thinner southeast part of the state to strike-slip faulting in the northwest. Whether the stress change is associated with the structure within the crust and/or upper mantle is difficult to tell. The pattern of reverse faulting continues down the eastern seaboard along the area of relatively thin crust. But reverse faulting in northern New York and southeastern Canada occurs with crust with more typical interior thicknesses. The pattern is slightly better matched with reverse faulting occurring above the regions of the relatively slow uppermost mantle (Figure S24), so perhaps the change (from South Carolina to Ottawa) is a result of an overall variation in lithospheric strength.

Cross-section G1-G2 (Figure S25) crosses eastern Ohio and through central Virginia and into northwestern North Carolina. Crustal thickness in eastern Ohio is comparable to that under the Appalachians, or perhaps slightly thinner. As discussed earlier in the Results section, the crustal thickness changes quickly as you exit the Appalachians to the east. Mantle speeds decrease modestly, but steadily from Ohio to the Appalachians. The 2011 M5.7 Virginia earthquake was located near an edge of a faster lower crust anomaly (the solid ellipse in Figure S25) and a change in crustal and upper mantle structure. Cross-section H1-H2 (Figure S25) crosses from the northeast WVSZ to the Charleston region and the South Carolina Seismic Zone. The crustal thickness increases slightly from the midwest into the Appalachians, and seismicity appears to extend slightly deeper in the

ETSZ near the profile. Near the southeastern margin of the Appalachians, into the coastal plain, the depth range of slower crustal material increases. The material that could be called lower-mid crust in the midwest and Appalachians disappears as the material with typical lower-crustal speeds shallows with a thinning of the crust. At the same position, the mantle speeds decrease along the east coast. Mantle speeds decrease modestly, but steadily from Indiana to the Appalachians, crossing the region that (Chu et al., 2013) suggested a hidden hot-spot track. Along the profile, we see no evidence for a slow upper mantle. However, our model includes a slight reduction in average upper mantle speed in northeast Kentucky and southwest Ohio (see Figure 6), directly above the turning points of the rays that showed delayed travel times and frequency-dependent amplitudes analyzed by (Chu et al., 2013) (the signals were generated by the Virginia earthquake and recorded on midwest Transportable Array stations described in that work). The slow upper mantle anomaly in our model is shallower than where they placed the anomaly but may reflect the same feature. However, we do not see it extend to the west, towards the northern Mississippi Embayment, as they suggested.

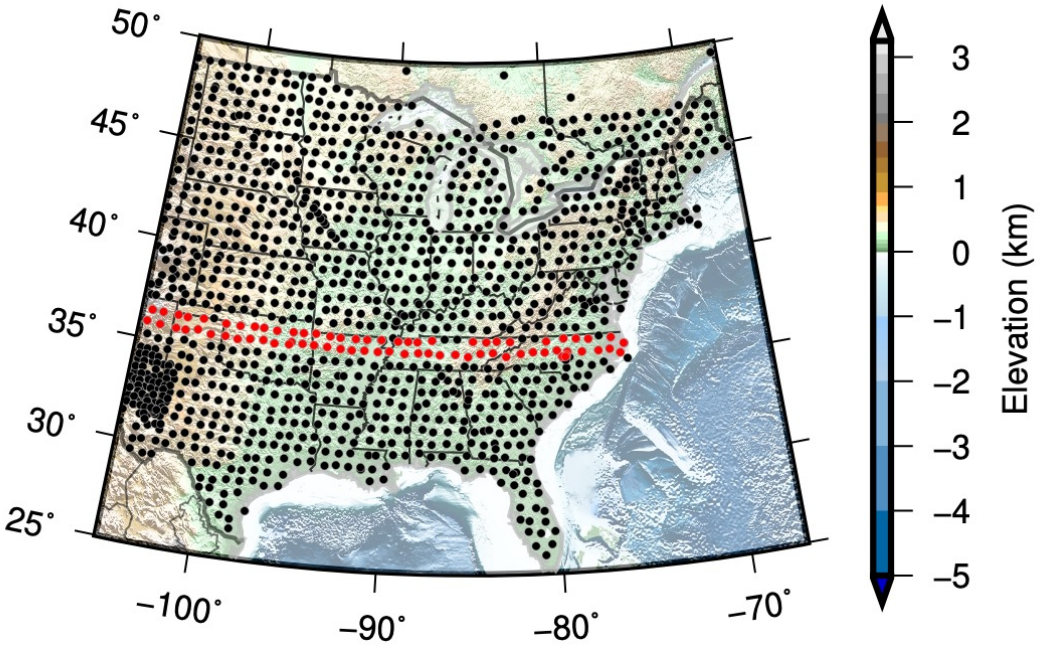

Figure S1. Map of the study region and seismic stations (dots) used in the receiver function wavefield smoothing/interpolation. Red dots show the stations used in Figure S6.

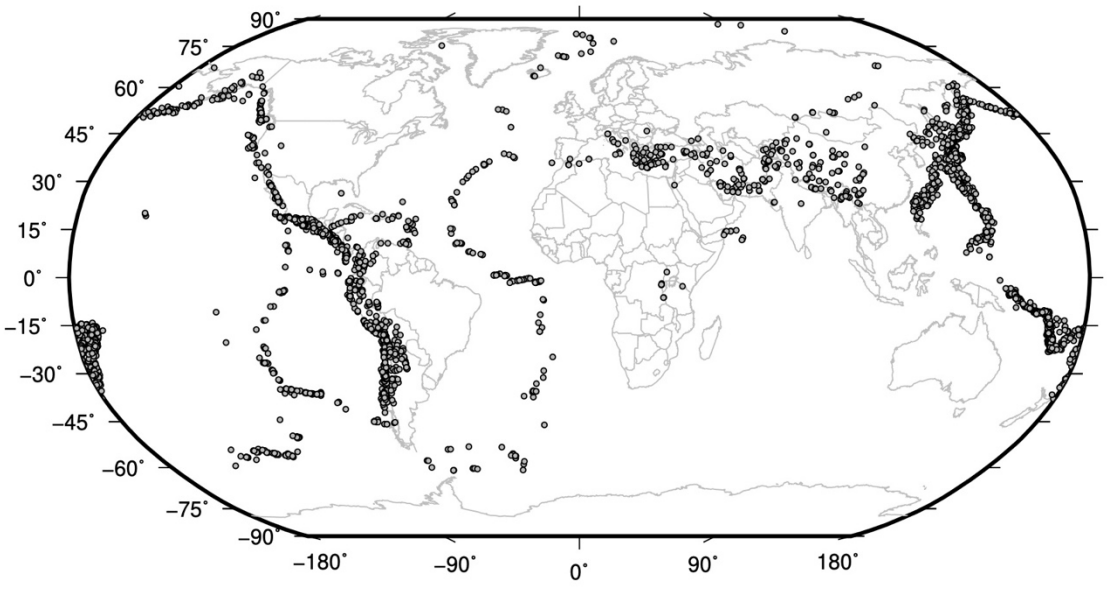

Figure S2. Seismic events (dots) used for the receiver function calculations.

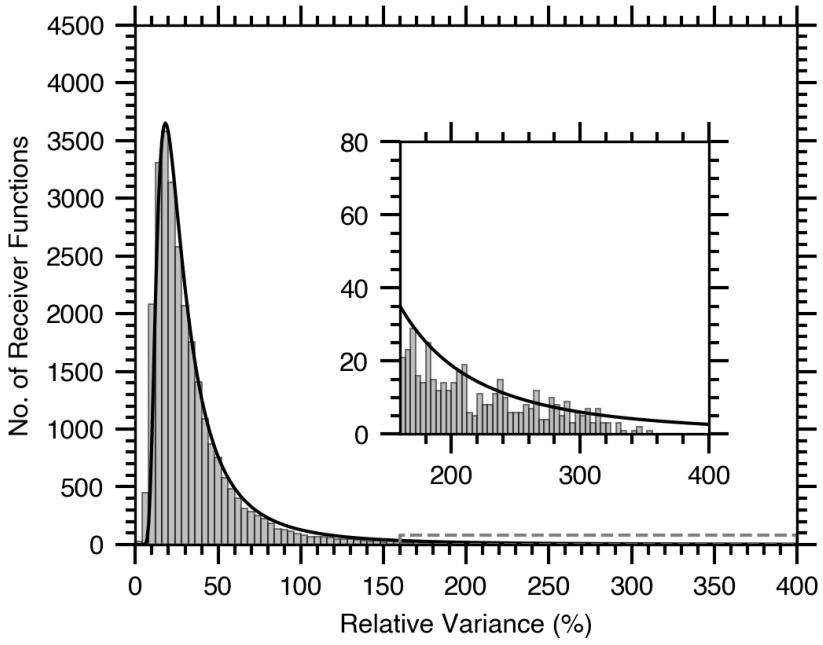

Figure S3. Relative data variance distribution of receiver functions recorded in the Eastern U.S. region. The insets show a detailed view for relative variance ranges between 165% and 400% (dashed box). Black lines indicate extreme value distributions. The relative data variance is computed as the signal variance between an individual receiver function and the single-station-averaged receiver function.

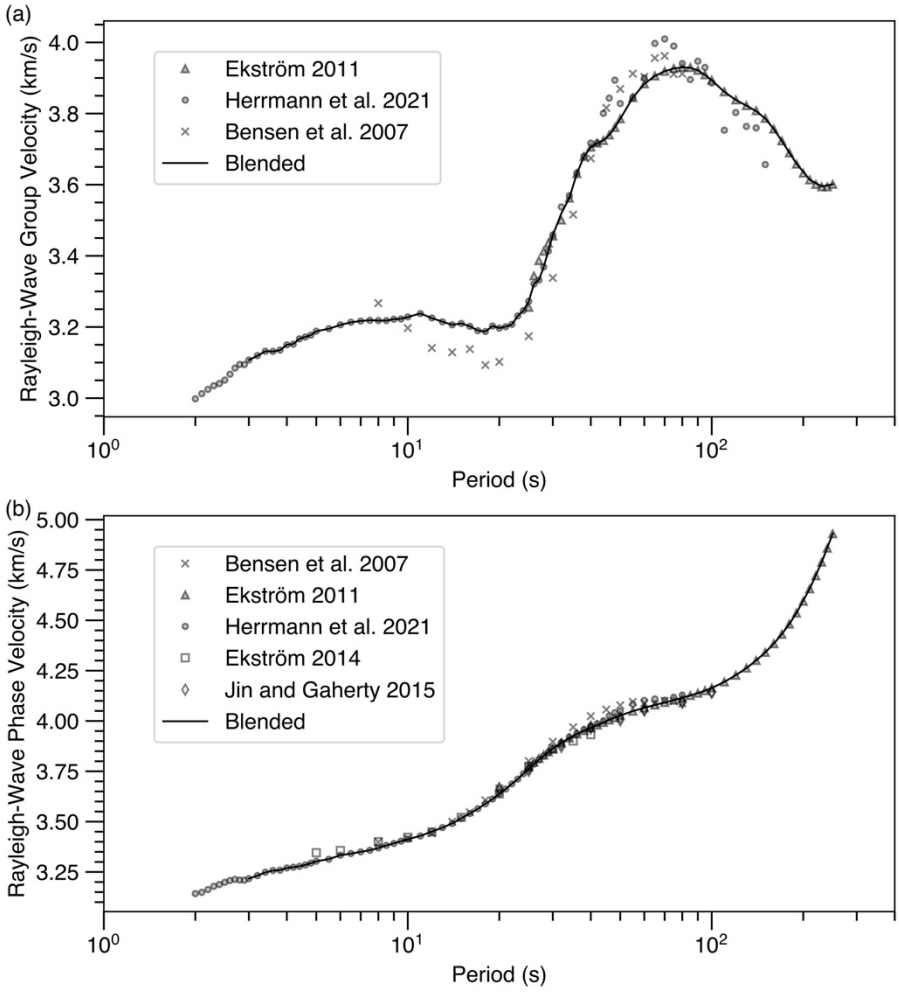

Figure S4. Example dispersion measurements and blended curves in the eastern U.S. (latitude 44.5˚N, longitude 73.5˚E) for (a) Rayleigh-Wave group velocity and (b) Rayleigh-Wave phase velocity. The blended curves were computed using values from Ekström (2011) and Herrmann et al. (2021). Dispersion models from other sources (Bensen et al., 2007; Ekström, 2014; Jin & Gaherty, 2015) are only shown for reference.

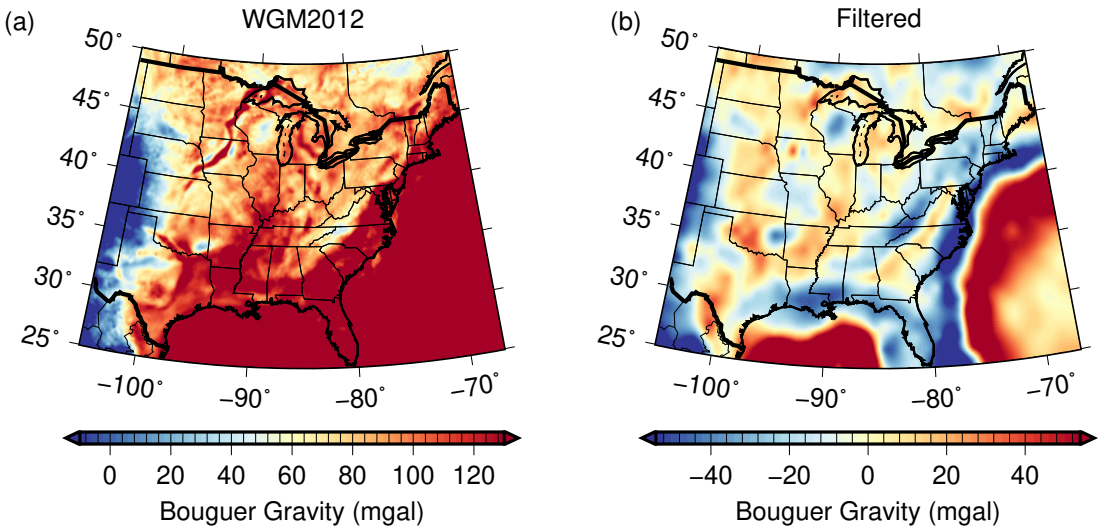

Figure S5. Bouguer gravity maps before (a) and after (b) wavenumber-filtering to emphasize gravity anomalies related to shallow structure and features have spatial dimension larger than 1˚. Note the color scale changes.

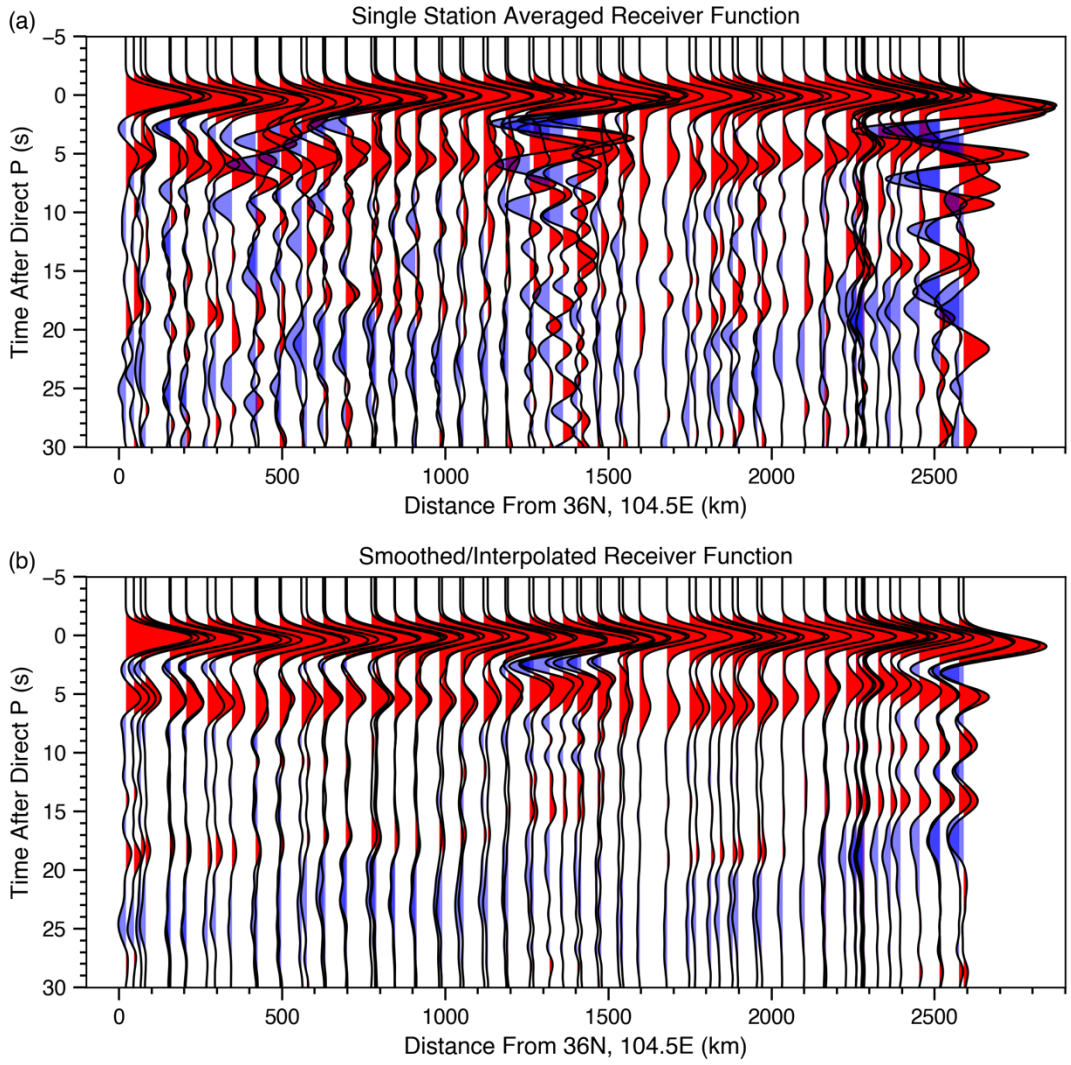

Figure S6. A comparison of (a) single station averaged and (b) smoothed/interpolated receiver functions in a cross-section view. The locations of the stations used are shown in Figure S1.

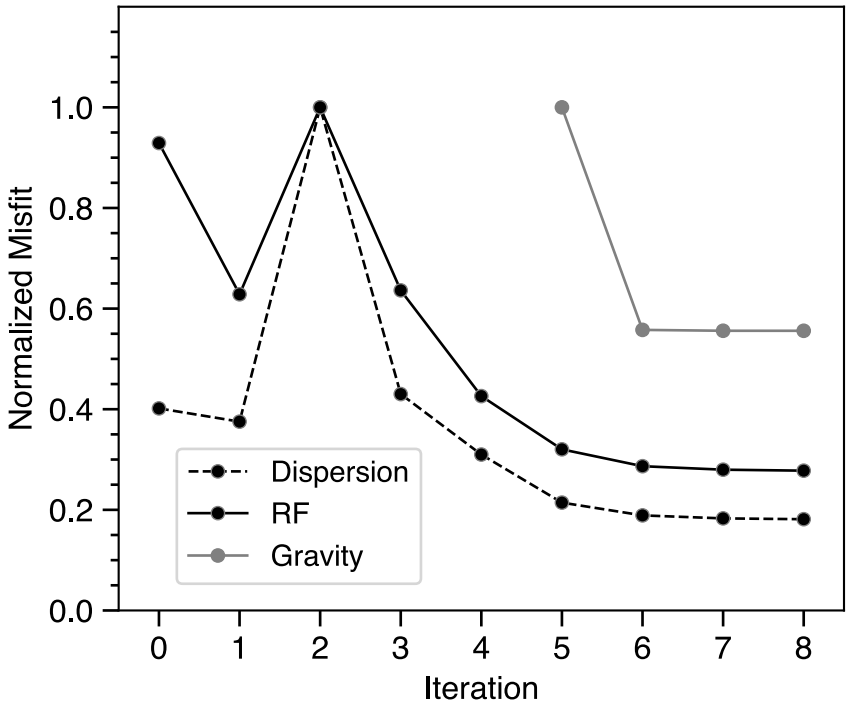

Figure S7. Convergence of the simultaneous inversion. The gravity observations were included in the last three iterations. Misfits for each type of observations are normalized with the maximum. For each iteration, misfits were averaged over the entire grid. At each grid location, dispersion misfit was averaged between group and phase velocity measurements while receiver function misfit was averaged from all available receiver functions. RF stands for receiver function.

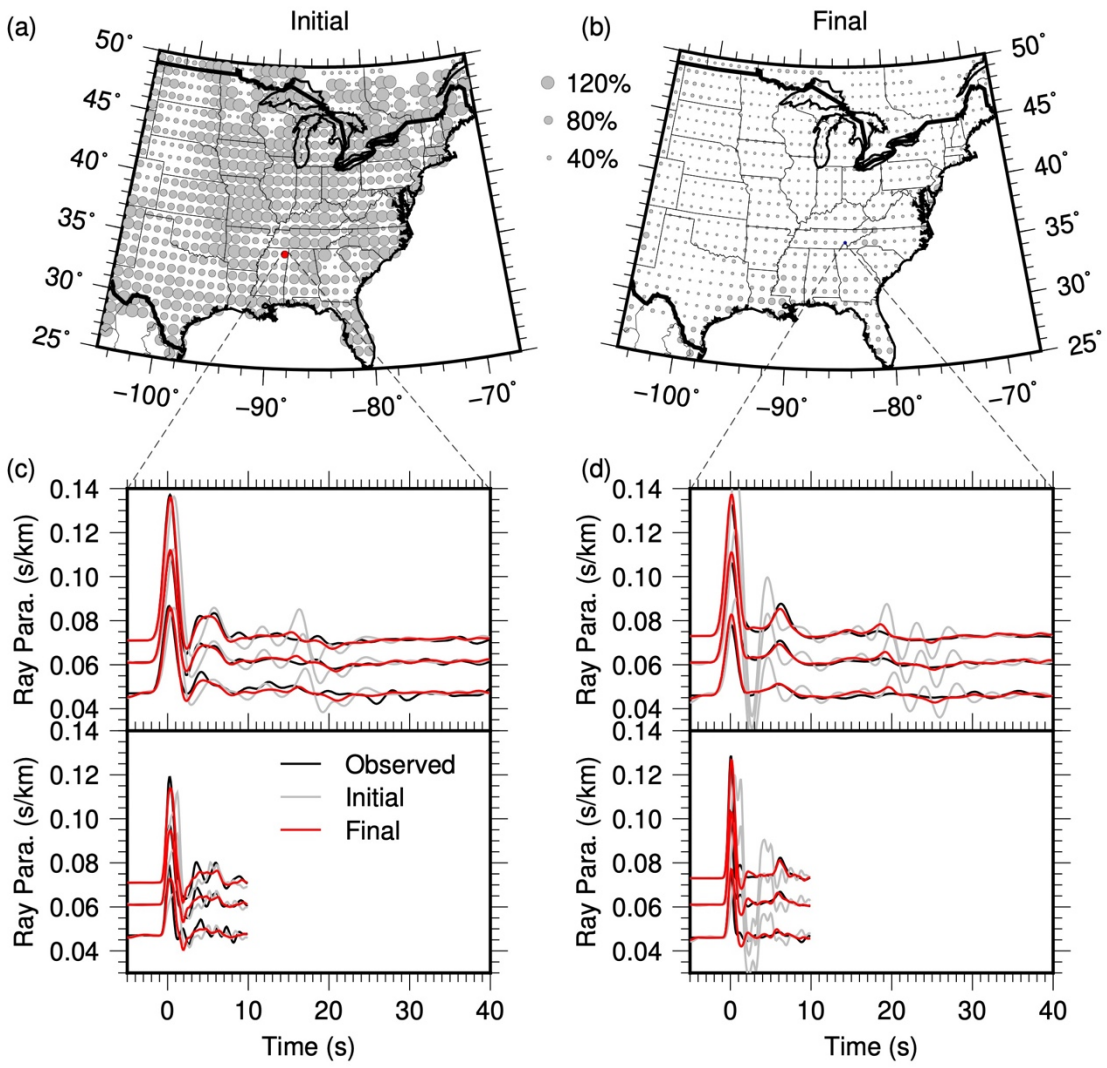

Figure S8. Maps showing the spatial distribution of receiver-function misfits for (a) the initial model and (b) the final model. The size of dots represents the normalized misfit at each grid point. Receiver functions at two grid points, (34.5˚, -88.5˚) and (35.5˚, -84.5˚), are showing in (c) and (d) with the locations indicated by the dashed black lines. Receiver functions with different ray parameters are displayed for both the narrow-band (Gaussian 1.0, top frame) and the broad-band (Gaussian 2.5, bottom frame). Since the broad-band receiver functions are noisier, we used a shorter time window.

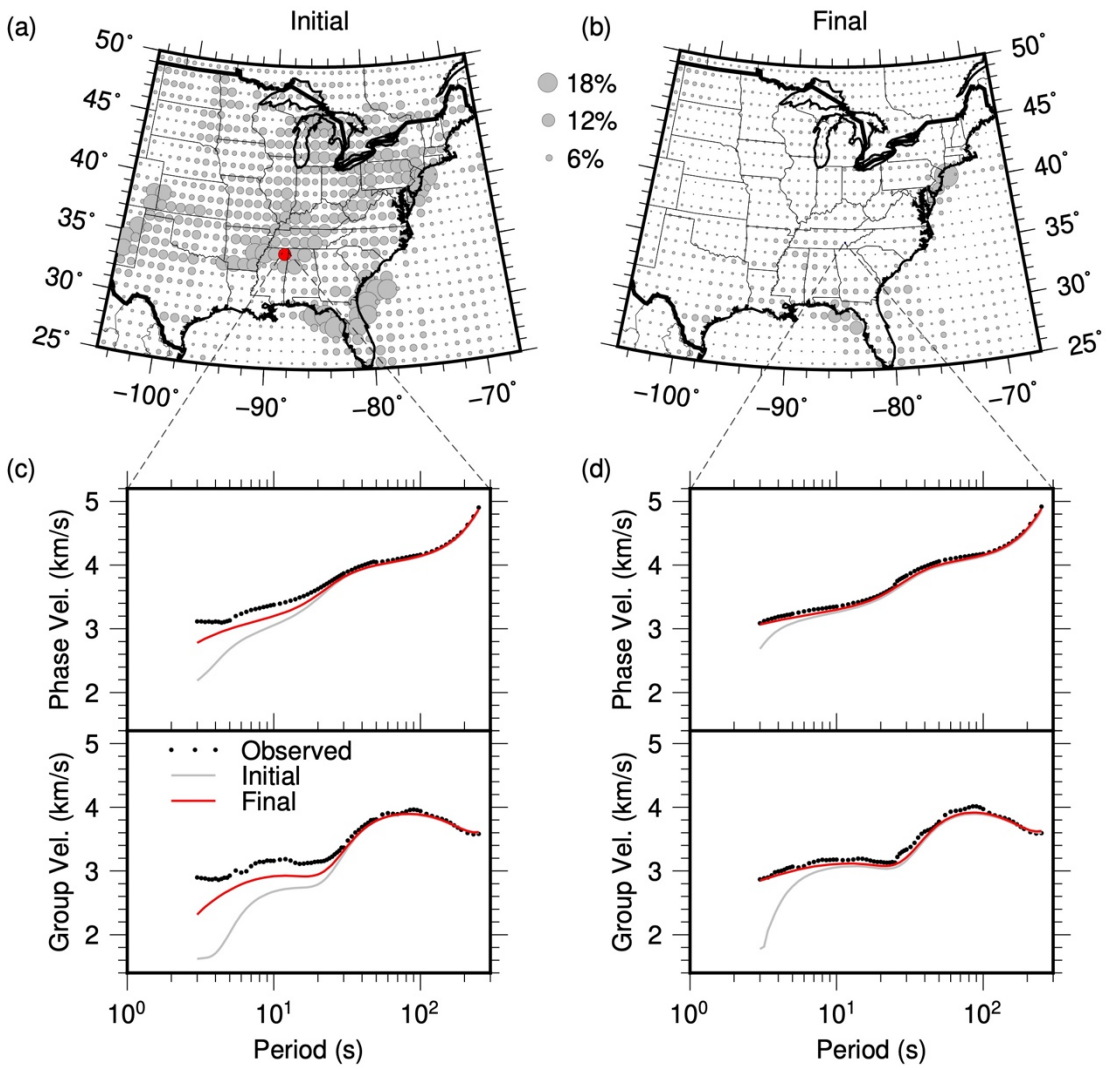

Figure S9. Maps showing the spatial distribution of the surface-wave dispersion misfits for (a) the initial model and (b) the inverted model. The size of dots represents normalized misfit at each grid points. Rayleigh-wave dispersion curves at two grid points, (34.5˚, -88.5˚) and (35.5˚, -84.5˚), are shown in (c) and (d) with the location indicated by the dashed black lines. The upper panel of (c) and (d) shows phase velocities while the lower panel shows group velocities.

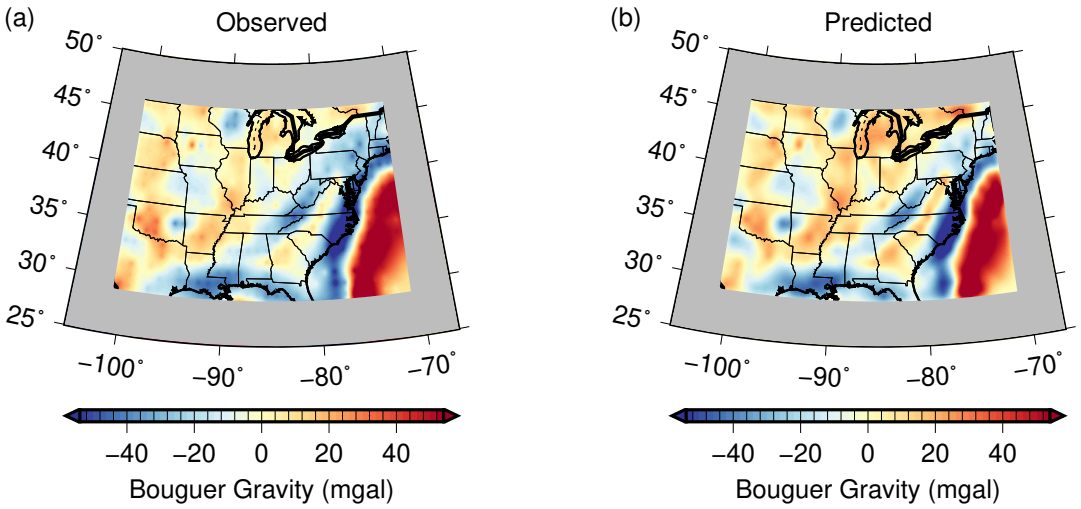

183

184 **Figure S10. A** comparison of (a) the observed gravity against (b) the predicted gravity for the
185 eastern U.S.

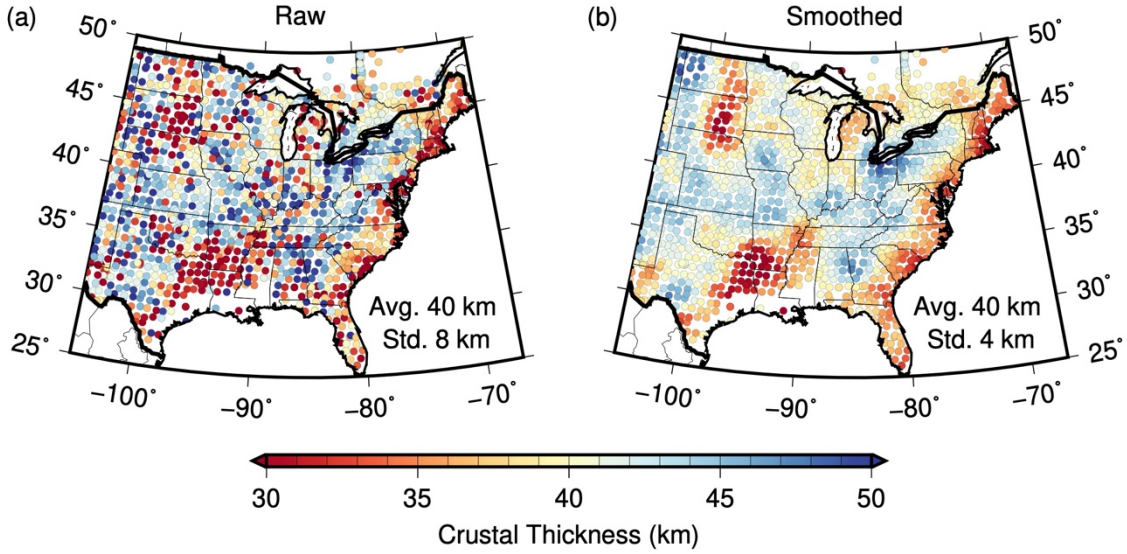

186

187 **Figure S11.** A comparison of EARS crustal thickness results (Crotwell & Owens, 2005) from (a)
188 the raw data and (b) the spatially smoothed version.

189

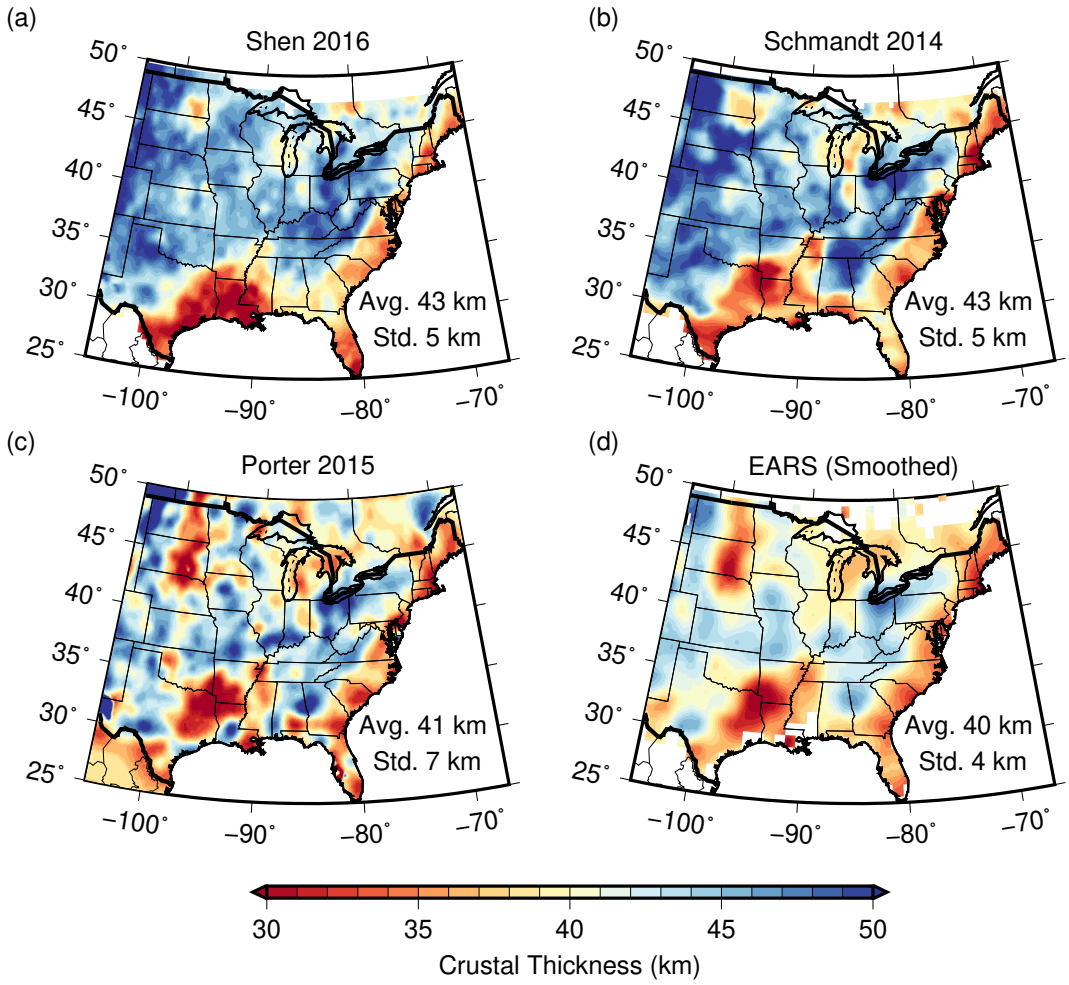

Figure S12. A comparison of crustal thickness maps from four recent models, (a) Shen-2016 model (Shen et al., 2016), (b) Schmandt-2014 model (Schmandt et al., 2015), (c) Porter-2015 model (Porter et al., 2016), and (d) the smoothed EARS model (Crotwell & Owens, 2005). The results of this paper are shown in Figure 5.

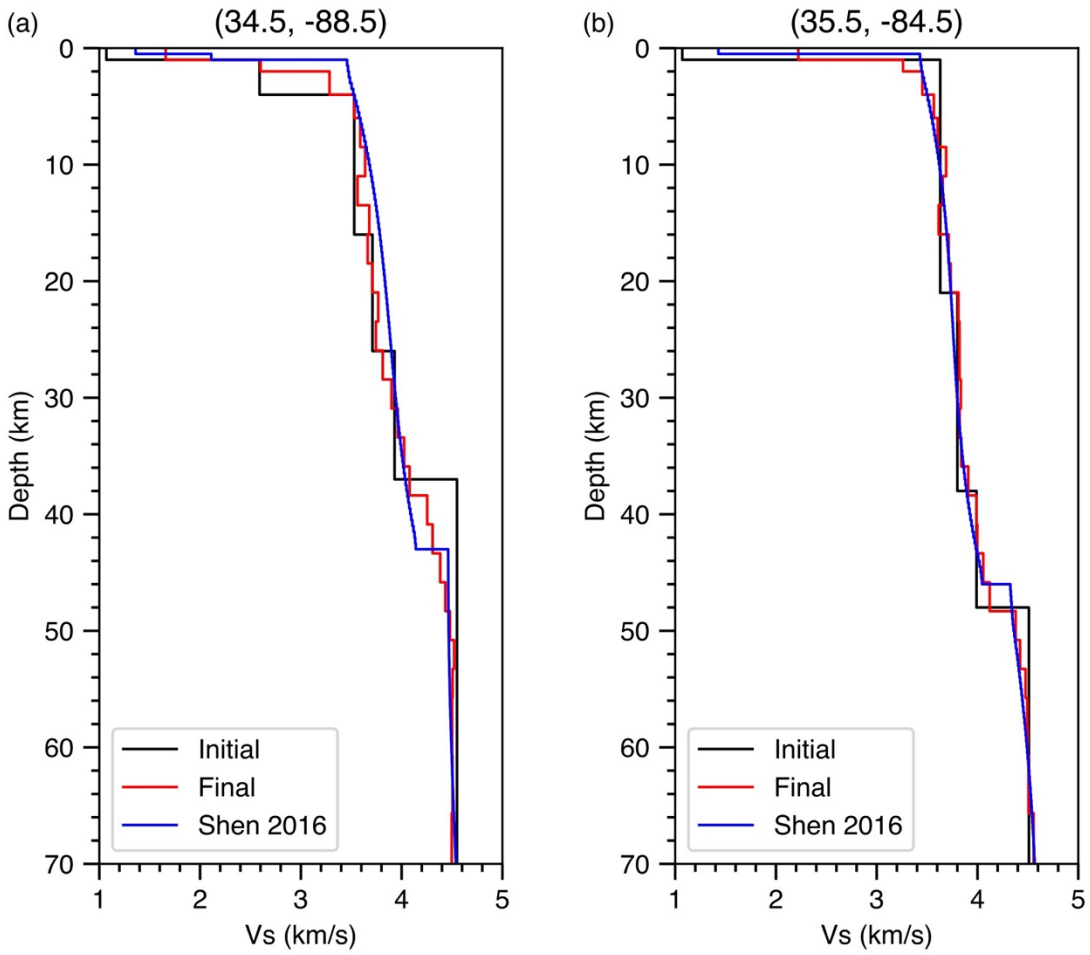

Figure S13. A comparison of 1D shear-wave velocity profiles at two grid points. The Shen-2016 model is extracted from Shen et al. (2016). The initial model is obtained from Crust 1.0. Correspoinding receiver functions and surface-wave dispersions can be found in Figure S8 and S9, respectively.

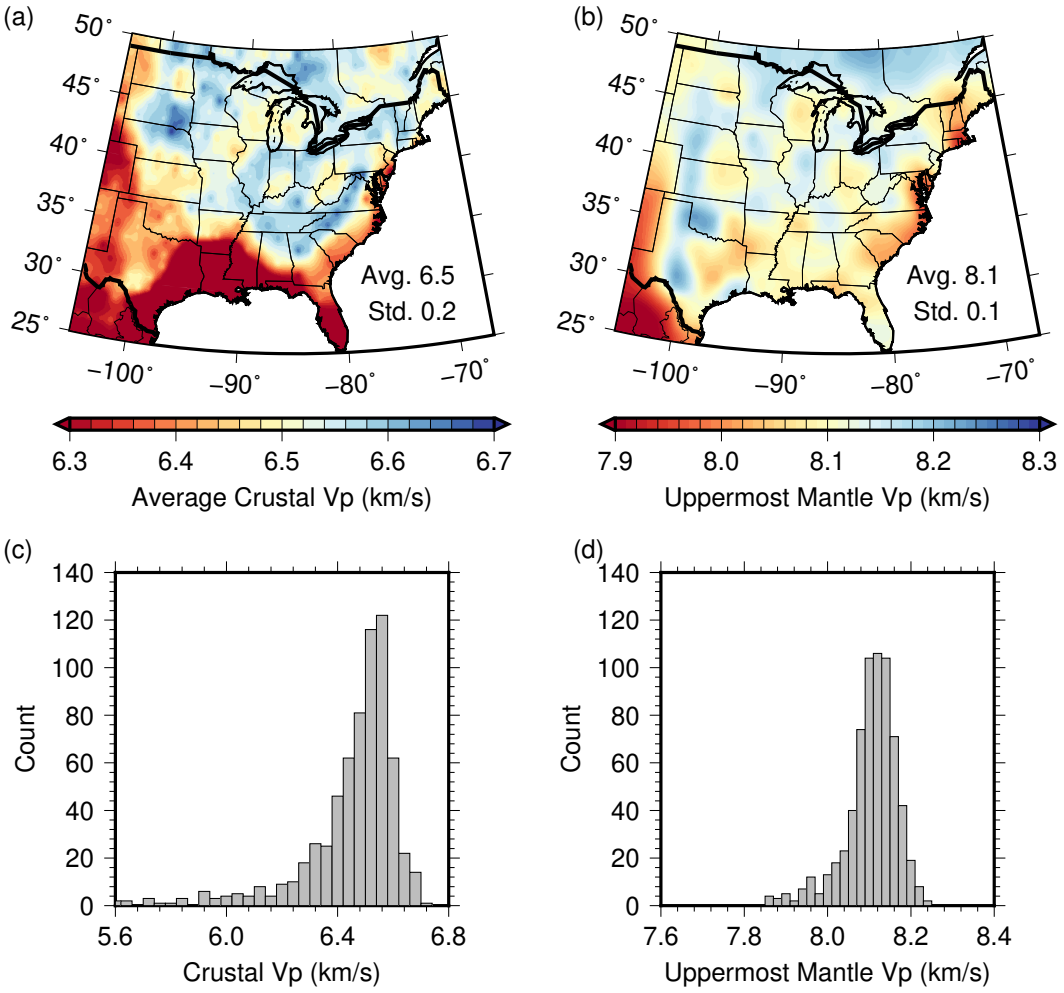

Figure S14. Maps showing (a) the averaged crustal V_p velocities, (b) uppermost mantle Vp velocities and histograms of (c) crustal and (d) uppermost mantle V_p velocity.

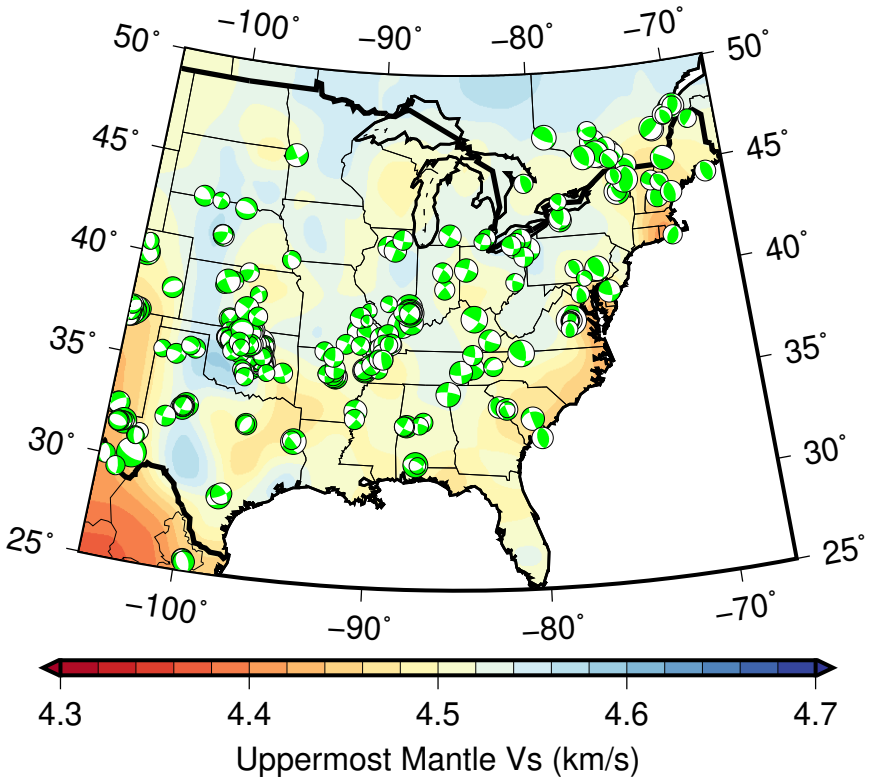

208

209 **Figure S15.** A comparison of the uppermost mantle V_s and focal mechanisms from the Saint
210 Louis University (SLU) catalog (prior 2021/05/01).

211

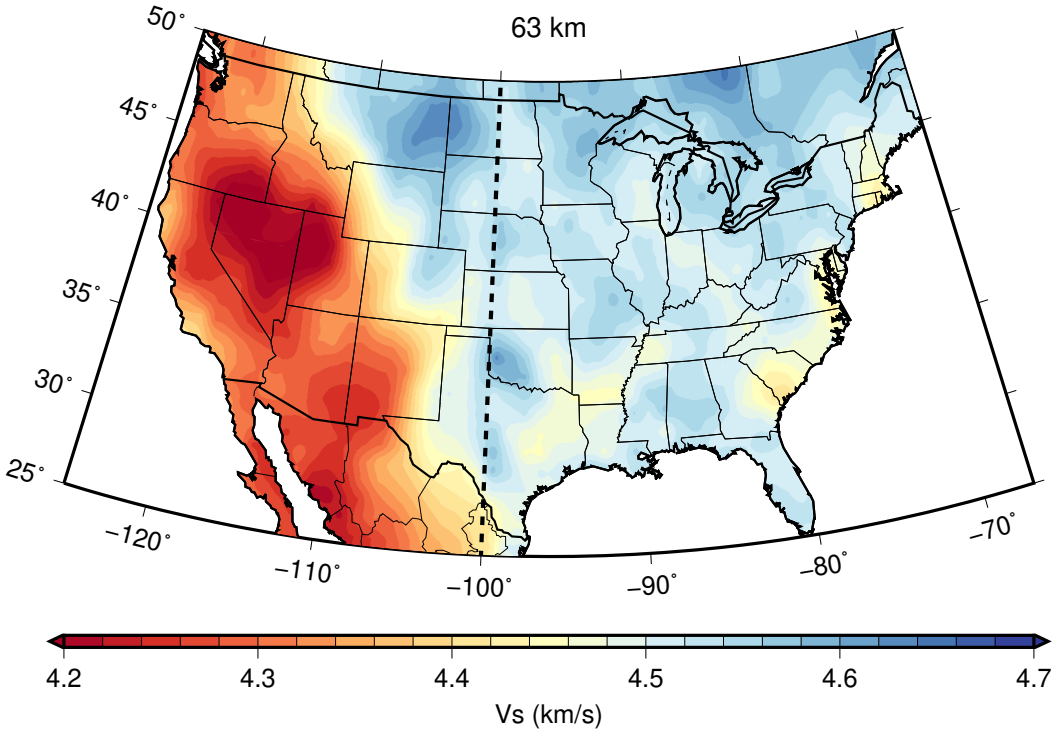

Figure S16. A comparison of the upper mantle shear speed at 63 km in western and eastern U.S. The dashed line indicates the transition from the western U.S. model (Chai et al., 2015) to the eastern U.S. model (this study).

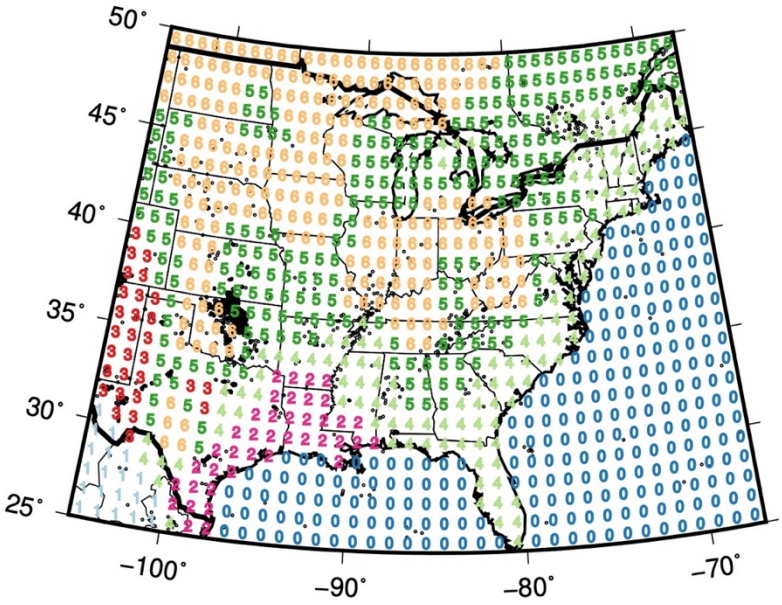

Figure S17. Spatial distributions of the automated model clusters generated using a simple hierarchical clustering algorithm. Similar 1D velocity profiles were grouped together as one cluster. Velocity profiles with large differences were assigned to different clusters. Each 1D velocity profile consists of shear velocities between 6 km and 200 km in depth. Note the oceanic profiles were assigned based on geographic location. The rough correspondence of the clusters to geologic regions are (0) Oceanic; (1) Southern Basin and Range Region; (2) Western Mississippi Embayment; (3) Central Basin and Range Region; (4) Atlantic Plain and Northern Appalachian Highlands; (5) and (6) Interior Plains, Central and Southern Appalachian Highlands, and Southern Canadian Shield. The velocity profiles within each cluster are summarized in Figure S18. Cirlces represent seismic events with a magnitude larger than 3 from the USGS NEIC catalog before May 2021.

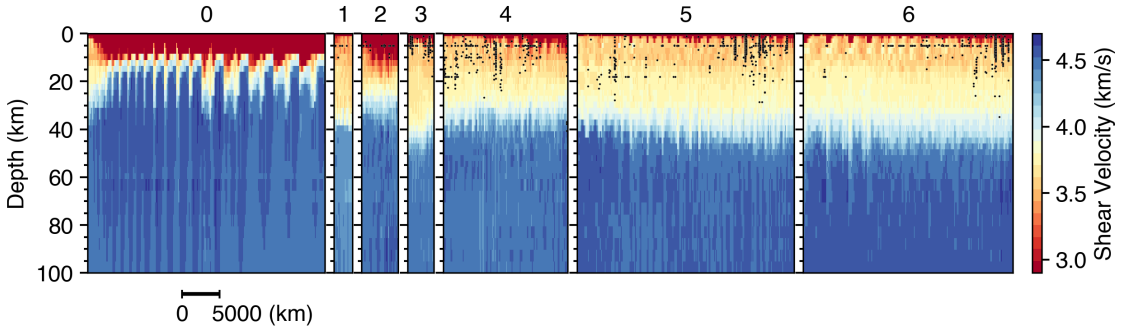

Figure S18. Shear velocity profiles of Earth model clusters corresponding to Figure S17. Each 1D velocity profile consists of shear velocities between 6 km and 200 km in depth. The label above each panel corresponds to a cluster in Figure S17. In each panel, individual 1D shear velocity profiles belong to the cluster are shown. Velocity profiles within the cluster are sorted from north to south by row (like in a book). Dots shows seismicity (magnitude 3 and larger) from the USGS NEIC catalog before May 2021.

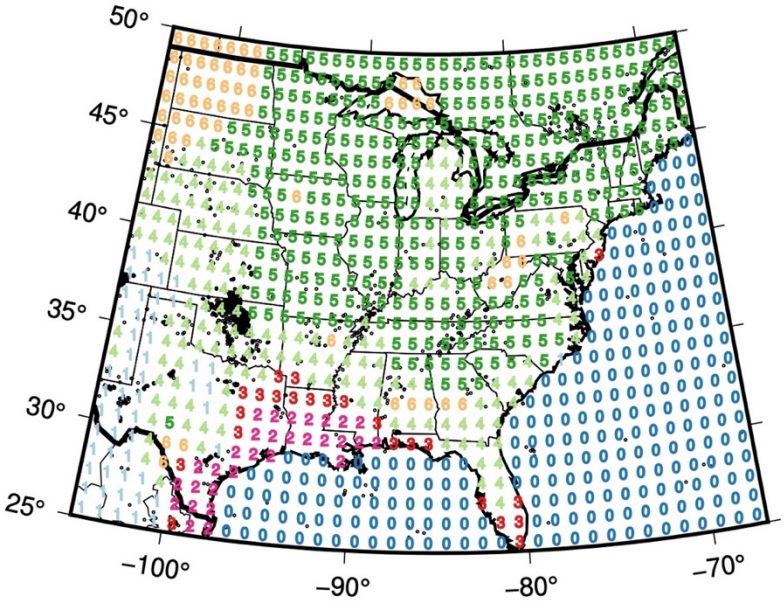

238

239 **Figure S19**. Same as Figure S17 but used the shear velocities of the upper 20 km.

240 .

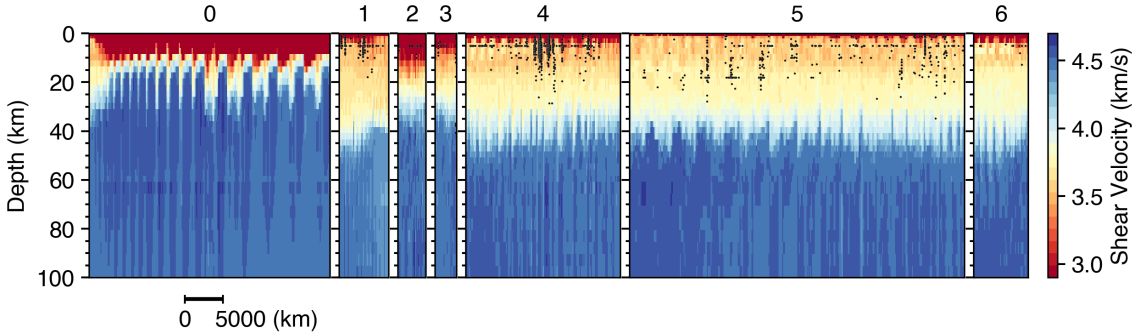

241

242 **Figure S20**. Same as Figure S18 but the clustering used the shear velocities of the upper 20 km.
243 The label above each panel correspond to that in Figure S19.

244

245

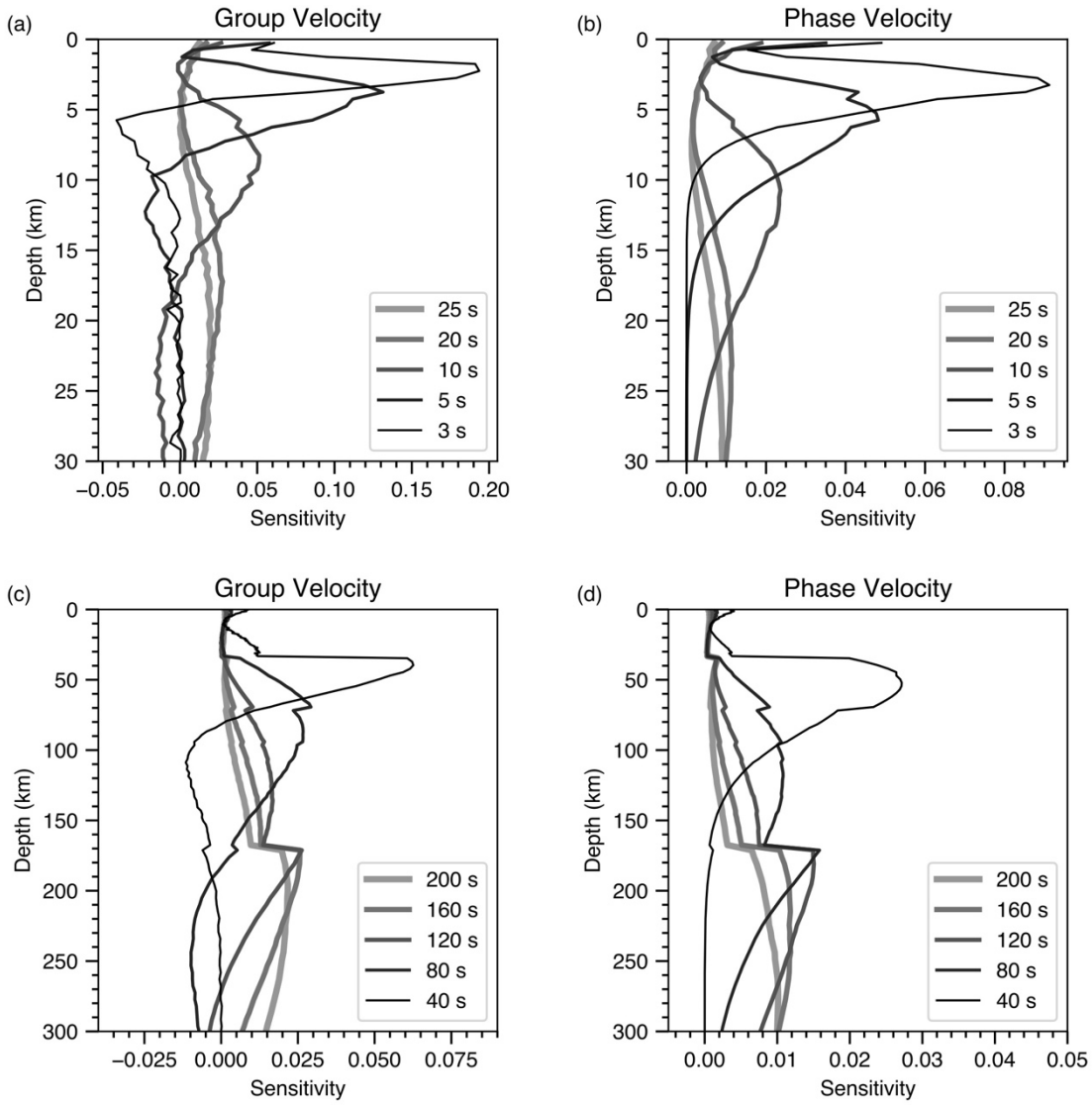

246

247 **Figure S21.** Rayleigh wave sensitivity to shear wave velocity.
248

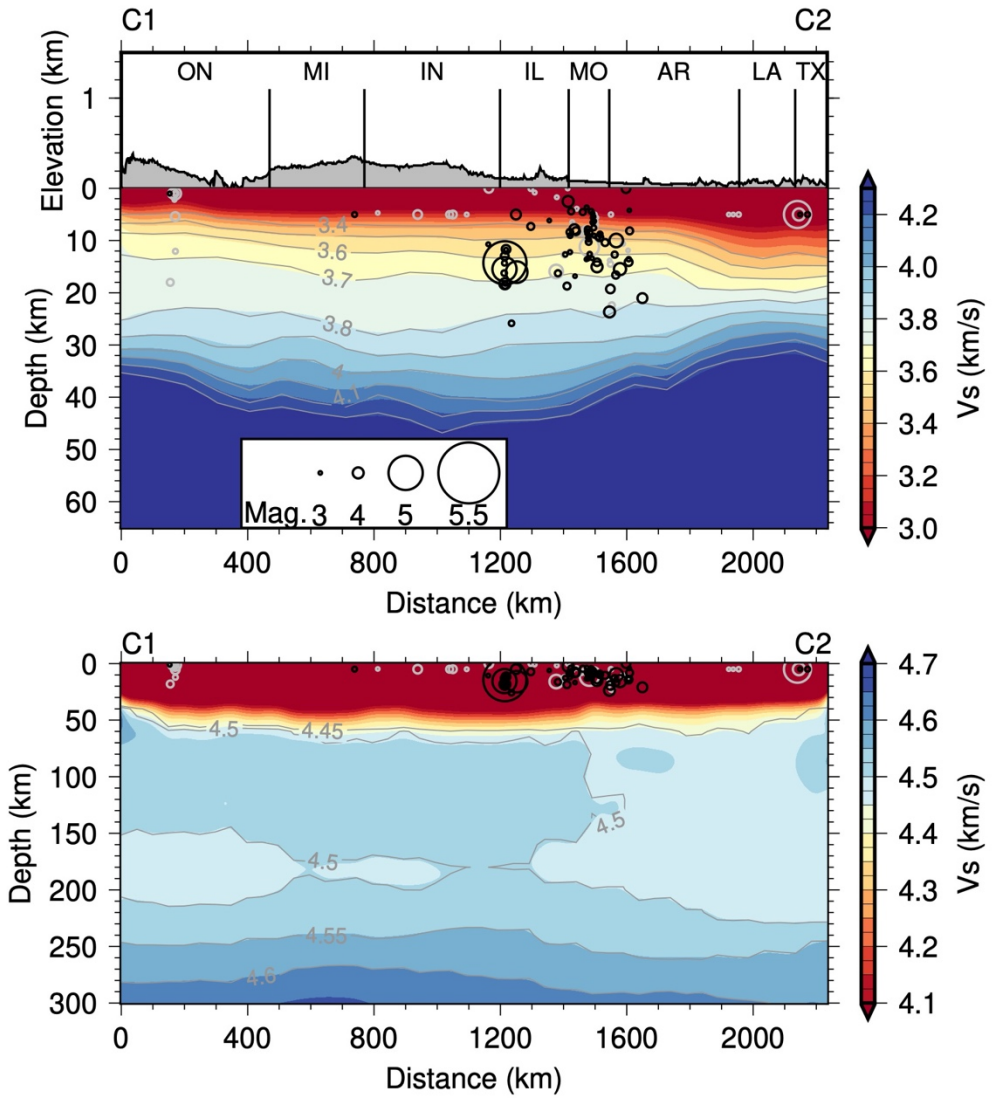

Figure S22. Shear velocity cross-sections along C1-C2. Top panel used a color palette that is suitable for crustal speeds. The lower panel shows shear-wave velocity using a color palette more suitable for mantle speeds. Circles are earthquakes located within 100 km of the cross-section. Black circles are events with depth uncertainties less than 5 km. Gray circles represent earthquakes with larger depth uncertainties or without uncertainties. Note the image is vertically exaggerated.

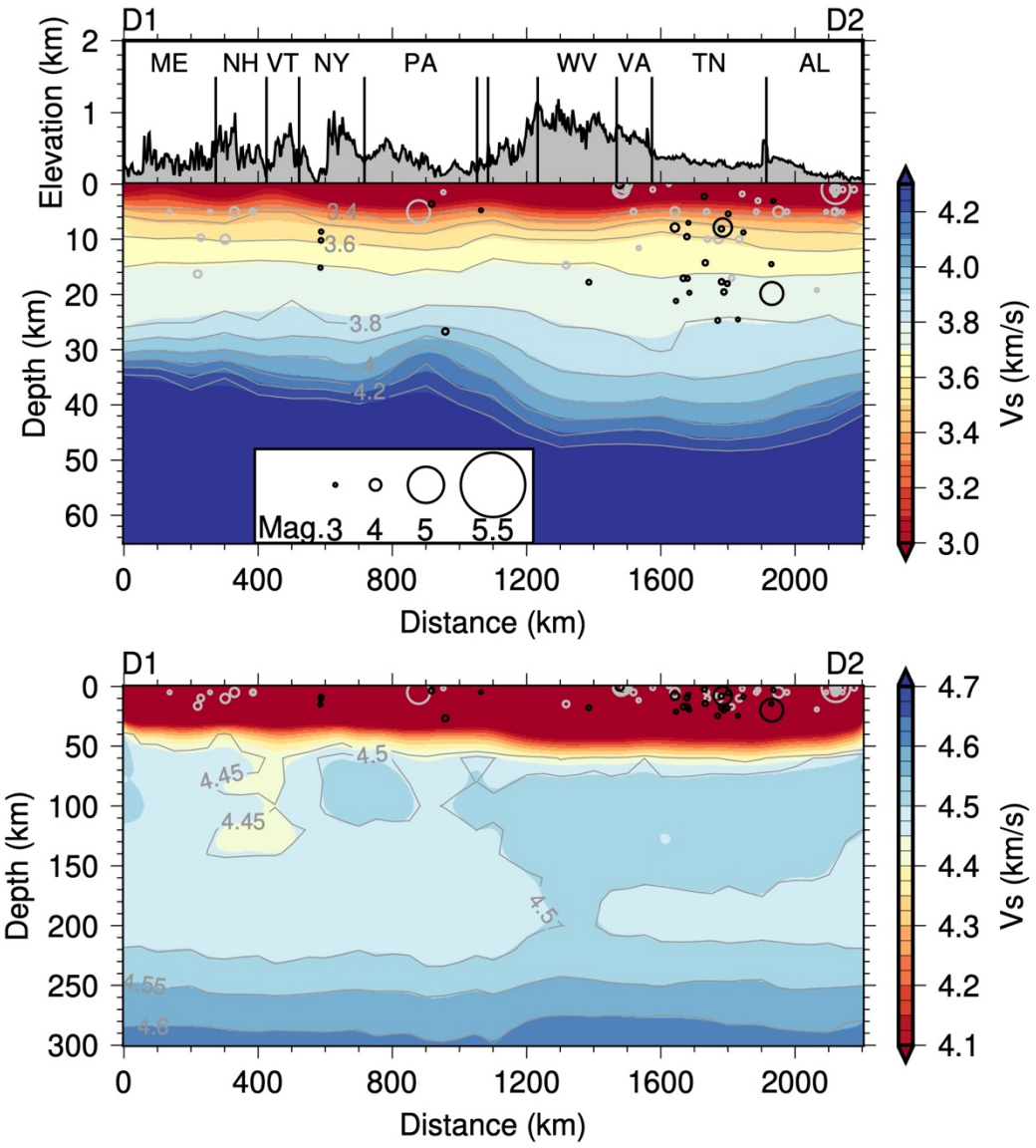

257

258 **Figure S23.** Same as Figure S22 but for cross-section D1-D2.

259

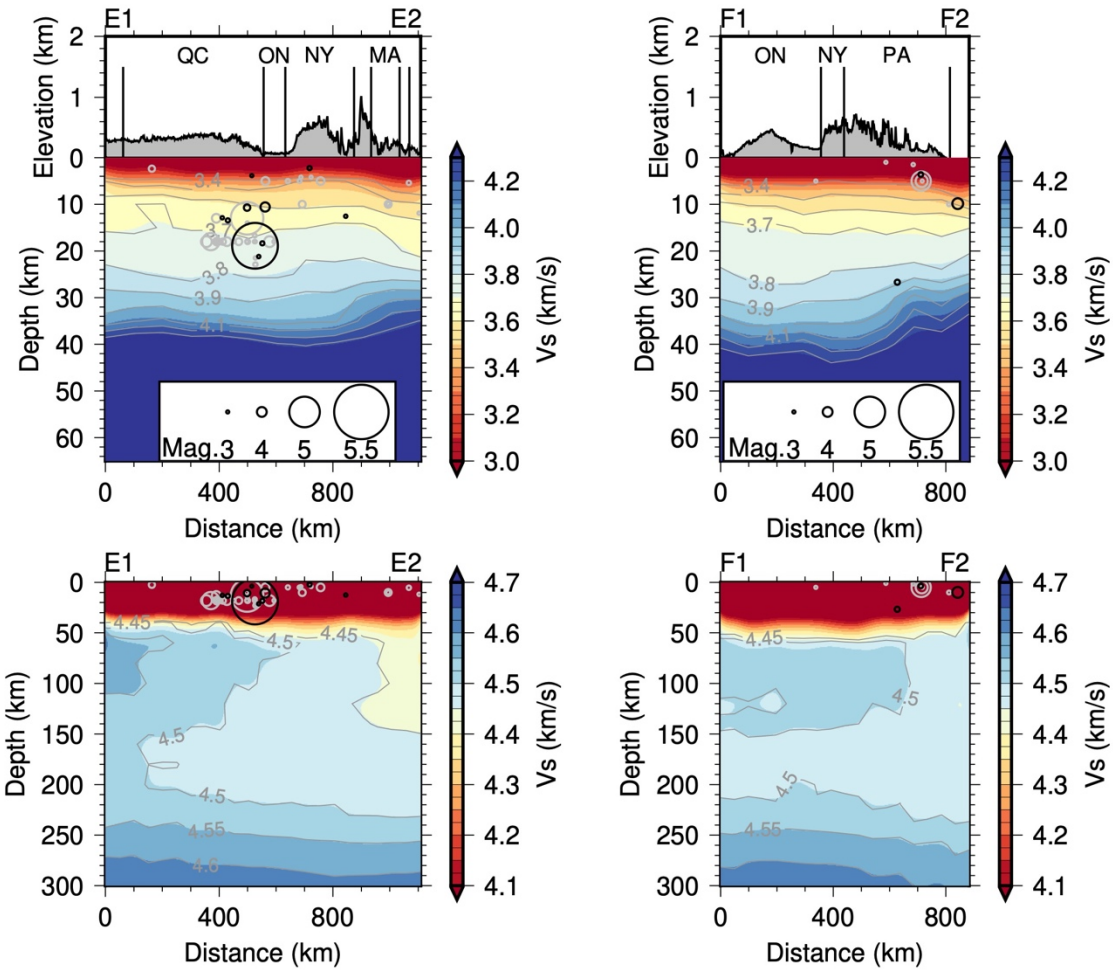

Figure S24. Same as Figure S22 but for cross-sections E1-E2 and F1-F2.

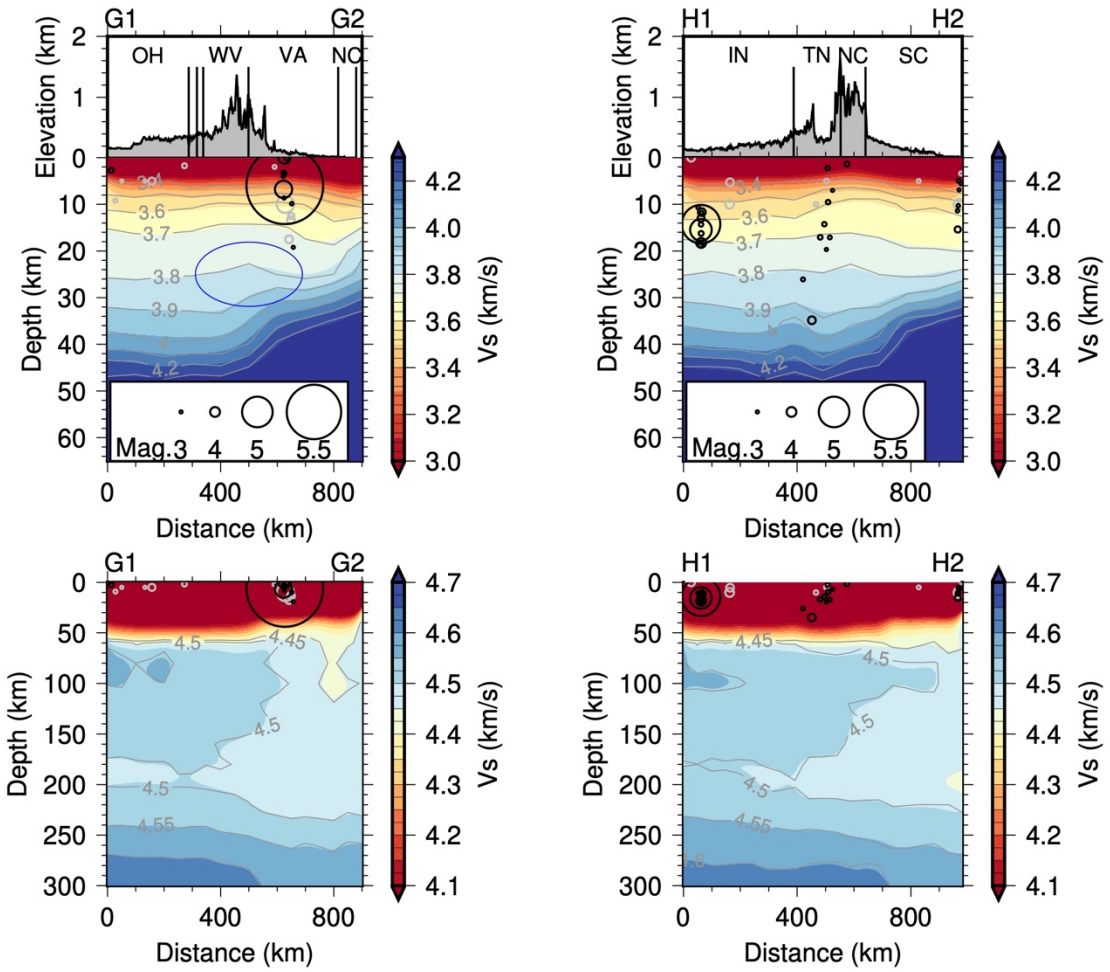

Figure S25. Same as Figure S22 but for cross-section G1-G2 and H1-H2. The solid ellipse incidates a faster lower curst anomaly.

Table S1. A list of seismic networks used for the receiver function calculation.

Data Set S1. The final seismic velocity model for the eastern United States derived from the inversion. The first column is latitude. The second column is longitude. The third column is depth (top of the cell) in kilometers. The fourth, fifth and sixth column are P-wave velocity (km/s), S-wave velocity (km/s), and density (g/cm^3), respectively.

Data Set S2. The seismic velocity model for the western United States from Chai et al. (2015). The first column is latitude. The second column is longitude. The third column is depth (top of the cell) in kilometers. The fourth, fifth and sixth column are P-wave velocity (km/s), S-wave velocity (km/s), and density (g/cm^3), respectively.

Movie S1. An animation compares the single-station-averaged receiver functions against the spatially smoothed/interpolated receiver functions.

Visualization S1. An interactive tool to view S-wave velocities of the 3D model for the eastern United States as depth slides and depth profiles side by side. The visualization was created with a Python script developed by Chai et al. (2018).

Visualization S2. An interactive tool to view S-wave velocities of the 3D model for the western United States (from Chai et al., 2015) as depth slides and depth profiles side by side. The visualization was created with a Python script developed by Chai et al. (2018).